University of Texas at El Paso
DigitalCommons@UTEP

Open Access Theses & Dissertations

2012-01-01

Applications of Density Functional Theory in Materials Science and Engineering

Manuel Alvarado
University of Texas at El Paso, malvarad7@gmail.com

Follow this and additional works at: https://digitalcommons.utep.edu/open_etd

 Part of the Materials Science and Engineering Commons, Mechanics of Materials Commons, Physical Chemistry Commons, and the Physics Commons

Recommended Citation
Alvarado, Manuel, "Applications of Density Functional Theory in Materials Science and Engineering" (2012). *Open Access Theses & Dissertations*. 2028.
https://digitalcommons.utep.edu/open_etd/2028

This is brought to you for free and open access by DigitalCommons@UTEP. It has been accepted for inclusion in Open Access Theses & Dissertations by an authorized administrator of DigitalCommons@UTEP. For more information, please contact lweber@utep.edu.

APPLICATIONS OF DENSITY FUNCTIONAL THEORY IN MATERIALS SCIENCE AND ENGINEERING

MANUEL ALVARADO Jr.

Materials Science and Engineering

APPROVED:

_____
Roy M. Arrowood, Ph. D., Chair

_____
Russell R. Chianelli, Ph. D.

_____
Philip C. Goodell, Ph. D.

_____
William Durrer, Ph. D.

_____
Benjamin Flores, Ph. D.
Interim Dean of the Graduate School

Copyright ©

by

Manuel Alvarado Jr.

2012

This dissertation is dedicated to my loving wife Mary Ellen Alvarado, whose love, compassion, and patience has helped guide me through every great undertaking in life.

APPLICATIONS OF DENSITY FUNCTIONAL THEORY IN MATERIALS SCIENCE AND ENGINEERING

by

MANUEL ALVARADO Jr., B.S., M.S.

DISSERTATION

Presented to the Faculty of the Multidisciplinary Program

in Materials Science and Engineering of

The University of Texas at El Paso

in Partial Fulfillment

of the Requirements

for the Degree of

DOCTOR OF PHILOSOPHY

Materials Science and Engineering

THE UNIVERSITY OF TEXAS AT EL PASO

August 2012

ACKNOWLEDGEMENTS

I would like to sincerely thank my dissertation advisor and mentor Dr. Roy Arrowood, whose guidance, knowledge, and patience helped me more than he will ever know. I would like to thank my research co-advisor Dr. Russ Chianelli for all his support and for the many interesting projects he gave me the privilege of participating in. I would like to extend my deep appreciation to the other members of my dissertation committee, Dr. Philip Goodell and Dr. William Durrer, for being so generous with their time and expertise.

I would like to thank the head of the Materials Science and Engineering department, Dr. Lawrence Murr for his leadership and for the generous use of the facilities within the department. I would like to thank the Associate Dean of Research and Graduate Studies, Dr. David Novick, for his help in securing support during the final stages of my dissertation.

I would like to thanks my colleagues at TXL Group, Dr. David Nemir, Dr. Jan Beck, and Mr. Ed Rubio, for giving me the privilege of working with them on so many interesting research projects.

I would also like to give thanks to the many members of Dr. Chianelli's group who were so helpful over the years, Dr. Brenda Torres, Dr. Manuel Ramos, and Mr. Hugo Lippmann.

Finally, I would like to thank my wife Mary Ellen Alvarado and all our children (Elizabeth, Michelle, Melinda, Alex, and Miranda) for being the source of my strength throughout this entire dissertation.

ABSTRACT

Density Functional Theory (DFT) is a powerful tool that can be used to model various systems in materials science. Our research applies DFT to two problems of interest. First, an organic/inorganic complex dye system known as a Mayan pigment is modeled to determine chemical binding sites, verifying each model with physical data such as UV/Vis spectra. Preliminary studies on palygorskite-based mayan pigments (mayacrom blue, mayacrom purple) show excellent agreement with experimental studies when using a dimer dye geometry binding with tetrahedrally-coordinated aluminum impurity sites in palygorksite. This approach is applied to a sepiolite-based organic/inorganic dye system using thioindigo attached to a tetrahedral aluminum impurity site with an additional aluminum impurity site in close proximity to the binding site. As a second application of DFT, various grain orientations in β-Sn are modeled under imposed strains in order to calculate elastic properties of this system. These calculations are intended to clarify discrepancies in published, experimental crystal compliance values.

TABLE OF CONTENTS

LIST OF FIGURES

LIST OF TABLES

Chapter 1

INTRODUCTION

The advances in electronic structure computational software have made first principles studies of solid state materials an extremely active field of research in materials science. Commercial packages today allow the calculation of the internal energies of molecules and crystals from basic quantum mechanics. Software packages such as Cerius[2], Gaussian, and Materials Studio provide a very simple interface through which properties such as lattice parameters, band structures, specific heats, optical and infrared spectra, elastic constants, and others can be calculated. These new tools are rapidly being used to study phase stability, diffusion, adsorption, catalytic behavior, and other fundamental materials properties.

The actual process of calculating these properties, while tempting, has been limited by the ability of the modeling software to be able to achieve these calculations in a reasonable amount of time and using computer resources which are commercially available. As a result, the initial attempts at developing a formalism for such calculations have been limited to binary systems at low temperatures and subject to a considerable amount of approximation, such as the application of a tight-binding approximation [1]. The evolution of Density Functional Theory (DFT), first introduced by Kohn and Sham in 1965 [2], presents an opportunity to overcome such limitations. DFT is a total energy method that employs an electron density functional instead of a many electron wavefunction in order to calculate the energy as well as various thermodynamic and electronic properties of a system of interest. Although this method still requires a nontrivial amount of computation the problem of calculating the energies of small molecules and crystals falls well within the ability of moderate-cost workstations to solve. It is this revolution in the development of computational methods that basis for our current study.

1.1 Density Functional Theory

The development of computational solid-state and quantum chemical software programs has always been severely hampered by the description of a potential of a many-electron system behaving according to Coulomb's Law (using atomic units):

$$V_{ee} = \frac{1}{2} \sum_{i} \sum_{i \neq j} \frac{1}{|\mathbf{r_i} - \mathbf{r_j}|}$$

An initial approach to this problem taken independently by Thomas[3] and Fermi[4] involved replacing the expectation value $\langle \mathbf{V}_{ee} \rangle$ by a direct Coulomb energy involving a functional of the electron number density $n(\mathbf{r})$:

$$\mathbf{U}[n] = \frac{1}{2} \int d^3\mathbf{r} \int d^3\mathbf{r}' \, \frac{n(\mathbf{r}) n(\mathbf{r}')}{|\mathbf{r} - \mathbf{r}'|}$$

A major problem remained, however, in the failure of the Coulomb energies to vanish for one-electron systems due to a spurious self-interaction in the energy. In addition to this problem, short-range Coulomb interactions involve the local environment around each individual atom which can result in deviations from the behavior predicted in the expectation values of the Coulomb potential. It is to address these problems that density functional theory (DFT) is employed.

Kohn and Sham[2] demonstrated that a density functional for a system of electrons can be expressed as functions of the electron density $\rho(\mathbf{r})$ for a system of natural electron spin orbitals ψ and occupation numbers a_n

$$\rho(\mathbf{r}) = \Sigma\, a_n \left|\Psi_n(\mathbf{r})\right|^2$$

which can then be substituted into the Kohn-Sham energy expression

$$\mathbf{E_{ks}}\,[\rho(\mathbf{r})] = \mathbf{T_s}[\rho(\mathbf{r})] + \mathbf{E_{es}}\,[\rho(\mathbf{r})] + \mathbf{E_{xc}}\,[\rho(\mathbf{r})] + \mathbf{E_{ext}}\,[\rho(\mathbf{r})]$$

where the individual terms refer to the kinetic energy of non-interacting electrons, the electrostatic energy between electrons, the exchange correlation energy, and the energy of electrons interacting with an external field $\mathbf{V_{ext}}$. The kinetic energy term can be expressed as

$$T_s = \sum_n a_n \left\langle \Psi_n \left| -\frac{1}{2}\nabla^2 \right| \Psi_n \right\rangle$$

The exchange correlation energy, which takes into account both the fictitious interaction between noninteracting particles (resulting from the Pauli exclusion principle) and the strong short-range correlation between electrons via mutual Coulomb repulsive forces, becomes a problematic functional. Kohn and Sham introduced the local density approximation (LDA) in order to estimate the effect of this functional. Assuming that the electron density is slowly varying this functional can be approximated by the expression

$$E_{xc}[\rho(\mathbf{r})] = \int \rho(\mathbf{r})\ e_{xc}(\rho(\mathbf{r}))\, d^3r$$

where $e_{xc}(\rho(\mathbf{r}))$ is the exchange and correlation energy of a homogenous electron gas of density $\rho(\mathbf{r})$. The advantage of this approach is that extensive values of $e_{xc}(\rho(\mathbf{r}))$ have been determined in previous theoretical quantum mechanical work. A serious shortcoming of this approximation is the failure of LDA to properly describe the binding forces in molecular systems in which the electron density cannot be considered to be slowly varying. To correct this effect Langreth et. al.[5] introduced the generalized gradient approximation (GGA) in which the exchange correlation energy is dependent on the spin polarization of electrons and is given by

$$E_{xc}[n\uparrow, n\downarrow] = \int f(n\uparrow, n\downarrow, \nabla n\uparrow, \nabla n\downarrow)\, d^3\mathbf{r}\,.$$

Such "semilocal" functionals derived from theoretical work have shown improvements over LDA approximations for molecular solids.

A recently developed method of DFT calculations for crystalline solids is the Cambridge Serial Total Energy Package (CASTEP) based on the work of Payne et al [6-8] and integrated into the Cerius[2] Molecular Dynamics software published by Molecular Simulations Inc. CATSEP employs a plane-wave pseudopotential approximation in order to describe electron orbitals and their interaction with an external potential. Using this approach, the external potential is written as a function of the free-atom density as the expression

$$V(\mathbf{r}) = \sum_j v(\mathbf{r} - \mathbf{r_j})$$

and the electron wavefunctions are written in terms of normalized plane waves as

$$|\mathbf{k}\rangle = \Omega^{-1/2} e^{-i\mathbf{k}\bullet\mathbf{r}}$$

here Ω is the volume of the crystal. Any eigenstate can then be expressed as

$$\Psi(\mathbf{r}) = \Sigma\, a_k |\mathbf{k}\rangle$$

These eigenstates can then be substituted into the Schrodinger equation

$$\frac{\hbar^2}{2m}\nabla^2\Psi + V(r)\Psi = E\Psi$$

and integrating over the volume Ω yields

$$\frac{\hbar^2}{2m}(\mathrm{k}')^2 a_{\mathrm{k}'} + \sum \langle \mathbf{k}' | V | \mathbf{k} \rangle a_k = E\, a_{\mathrm{k}'}$$

The problem is now reduced to a set of simultaneous linear equations which couple the a_k coefficients for **k** differing from **k´** by a lattice parameter. This may be seen by writing out the matrix element of V as

$$\langle \mathbf{k}' | \mathbf{V} | \mathbf{k} \rangle = \frac{N}{\Omega_0} \sum e^{-i(\mathbf{k}' - \mathbf{k})\cdot \mathbf{r}_j} \int \mathbf{e}^{-i(\mathbf{k}' - \mathbf{k})\cdot(\mathbf{r} - \mathbf{r}_j)} v(\mathbf{r} - \mathbf{r}_j) \, d^3\mathbf{r}$$

where Ω_0 is the atomic volume of the crystal and N is the structure factor of the crystal. The problem is then reduced to a relatively simple sum over atomic positions in the crystal structure. The resulting computations will then yield the total electronic energy of a given structure as well as its band structure and density of states.

A major drawback of this plane wave approach is that a plane wave basis set is poorly suited to expanding the electronic wavefunctions unless a very large number of plane waves are employed in order to model the rapidly oscillating wavefunctions of the core electrons. In reality, most physical properties of the solid state are dependent on valence electrons to a much greater degree than core electrons. The pseudopotential approximation is employed in order to remove core electron and nuclear potential contributions to the total electronic energy, instead replacing these terms with a weaker pseudopotential which acts on a set of pseudo wavefunctions rather than on the true valence wavefunctions.

In order to generate a pseudopotential the all electron eigenvalues of an atom must be determined using the previously used Schrodinger equation

$$\left\{ -\frac{\hbar}{2m} \nabla^2 + V \right\} \Psi_{AE_t} = c_\ell \Psi_{AE_t}$$

where Ψ_{AE} is the wavefunction for the all electron atomic system with angular momentum component ℓ. The resulting valence eigenvalues are substituted back into the Schrodinger equation but with a parameterized pseudo wavefunction of the form

$$\Psi_{pst} = \sum_{i=1}^{n} \alpha_i j_l .$$

Here, j_l are spherical Bessel functions (generally, only three or four are needed for most pseudopotentials) and α_i are coefficients fitted to the following conditions:

1. The core charge produced by the pseudo wavefunctions must be the same as that produced by the atomic wavefunctions.
2. Pseudo electron eigenvalues must be the same as the valence eigenvalues obtained from the atomic wavefunctions.
3. Pseudo wavefunctions and their first and second derivatives must be continuous at the core radius and non-oscillatory.
4. On inversion of the all electron Schrodinger equation of the atom excited states may also be included in the calculation.

The two main classes of pseudopotentials are norm-conserving and ultrasoft. Norm-conserving pseudopotentials, designed mainly to accurately generate identical charge densities when compared to the real potentials, will satisfy the condition

$$\int_0^{r_c} \psi^*_{AE}(r)\, \psi_{AE}(r)\, dr = \int_0^{r_c} \psi^*_{ps}(r)\, \psi_{ps}(r)\, dr$$

where $\psi_{AE}(r)$ is the all electron wavefunction and $\psi_{ps}(r)$ is the pseudo wavefunction. These pseudopotentials guarantee the equality of the all electron and pseudo wavefunctions outside of the core region. On the other hand, ultrasoft pseudopotentials attain much smoother (softer) pseudo wavefunctions and thus use considerably fewer plane waves for calculations of the same accuracy. This method partitions the total valence density n(r) into "hard" and "soft" contributions

$$n(r) = \sum_n \left[|\phi_n(r)|^2 + \sum_{i,j} Q_{ij}(r)\, \langle \phi_n \mid \beta_j \rangle \langle \beta_i \mid \phi_n \rangle \right]$$

where β_i are projector functions that depend on ionic positions and $Q_{ij}(r)$ is the augmentation function given by

$$Q_{ij}(r) = \psi_i^*(r)\, \psi_j(r) - \phi_i^*(r)\, \phi_j(r),$$

for $\psi_j(r)$ all electron wavefunctions and $\phi_i(r)$ ultrasoft pseudo wavefunctions. These are constructed without satisfying the norm conservation condition $Q_{ij}(r) = 0$. The cutoff energy (E_{cut}) for ultrasoft pseudopotentials is about half of that for norm-conserving pseudopotentials. As the number of plane waves scales as $E_{cut}^{3/2}$ approximately one third less plane waves are used in the ultrasoft case.

It should be noted that the results of these computations using CASTEP yielded very similar results for both LDA and GGA exchange correlation functionals when using the same pseudopotential, which is a reasonable result as differences between the two methods should become most pronounced when examining molecular solids as opposed to crystalline metals.

1.2 Molecular Orbital Theory

While DFT proves to be an extremely powerful tool when calculating optimized structures and energies there is no consideration given to the interactions due to atomic orbitals. As such, the modeling of interactions dominated by orbitals (such as bond enthalpies, molecular dipole moments, and UV/visible spectra) requires the application of molecular orbital (MO) theory. The following approach follows the same convention used by Huckel in his initial formulation of MO theory[9] and later refined by Pople, Zunger, and other more recent work [10,11].

MO theory, like DFT, seeks to find a solution to the Schrodinger equation. This is done by applying three basic simplifications:

(a) ***Born-Oppenheimer approximation***: the wavefunction of a molecule can be uncoupled into nuclear and electronic contributions.

$$\Psi_{\text{total}} = \Psi_{\text{electronic}} \times \Psi_{\text{nuclear}}$$

The advantage of this approach is that the nuclear positions, which affect the electrons in terms of an electrostatic potential, can often be assumed to consist of an equilibrium configuration. Additionally, the kinetic energies of nuclei are assumed to be negligible compared

to electronic kinetic energies (due to the large mass discrepancies between electrons and atomic nuclei. We then have two separate Schrodinger equations as a result of the uncoupling, with the electronic and nuclear Hamiltonians being given by

$$\hat{H}_e = -\frac{1}{2}\sum_i \frac{\nabla_i^2}{m_i} - \sum_{A,i} \frac{Z_A}{r_{Ai}} - \sum_{i>j} \frac{1}{r_{ij}}$$

$$\hat{H}_N = -\frac{1}{2}\sum_i \frac{\nabla_A^2}{M_A} + E_e(R) - \sum_{A>B} \frac{Z_A Z_B}{R_{AB}}$$

where the subscripts i and j are summed over electrons, A and B are summed over nuclei, and $E_e(R)$ is the electronic energy contribution from solving the electronic Schrodinger equation at nuclear coordinate R.

(b) ***Hartree-Fock approximation***: the electron-electron interaction is approximated by replacing the many-body electronic wavefunction by a wavefunction obtained from a single Slater determinant of N spin orbitals.

$$\Psi_E = \begin{vmatrix} \psi_1(x_1) & \psi_1(x_2) & \cdots & \psi_1(x_N) \\ \psi_2(x_1) & \psi_2(x_2) & \cdots & \psi_2(x_N) \\ \vdots & \vdots & & \vdots \\ \psi_N(x_1) & \psi_N(x_2) & & \psi_N(x_N) \end{vmatrix}$$

This replaces individual electron-electron interactions with interactions of each electron with an average non-local potential arising from the presence of all other electrons.

(c) ***Linear combination of atomic orbitals (LCAO)***: electronic positions within orbitals can be approximated by expanding each orbital into a linear basis set:

$$\psi_i = \sum_{\mu} c_{\mu i} \varphi_{\mu} ,$$

where φ_{μ} represents an atomic orbital wavefunction in the basis set. By convention the molecular orbitals are required to be orthonormal, thus requiring that

$$\sum_{\mu \upsilon} c^{*}_{\mu i} c_{\upsilon j} S_{\mu \upsilon} = \delta_{i j} ,$$

where δ_{ij} is the Kronecker delta function and $S_{\mu\upsilon}$ is the orbital overlap integral given by

$$S_{\mu\upsilon} = \int \varphi_{\mu}(1) \varphi_{\upsilon}(1) d\tau_1$$

for atomic orbital functions φ_{μ} and φ_{υ}. The advantage of this approximation is that a number of basis sets have been developed that model various systems with a good degree of accuracy. A serious limitation, however, is the need to evaluate a large number of electron repulsion integrals as a result of overlap between orbitals that comprise the linear basis set. As a result, different levels of approximation are used. In the Complete Neglect of Differential Overlap (CNDO)[12] approximation only valence orbitals are treated explicitly (frozen core) and the orbital overlap

integral is assumed to be negligible. As a result CNDO is known to fail when modeling systems in which separation of states resulting from the same configuration are significant, such as is the case with organic molecules. An alternative approximation, the Intermediate Neglect of Differential Overlap (INDO)[13] approximation, takes into account partial overlap. This is done by retaining terms in the orbital overlap integral $S_{\mu\upsilon}$ subject to the constraint that $\mu = \upsilon$. This results in better agreement with experimental values for organic molecules and other systems where overlap plays a significant role (N-H bonding, for example).

Chapter 2

PREVIOUS RESEARCH

2.1 Introduction

This section describes preliminary work done in applying computational methods to two problems. First, density functional theory was used to obtain and molecular orbital theory were used to simulate the organic/inorganic complex dye system known as maya blue. Second, density functional theory was used to obtain optimized lattice parameters (minimum energy) for the β-Sn structure. In both cases the computational results are verified using available published data. For DFT calculations, CASTEP was used, while for MO calculations VAMP was used. Both computational modules are bundled within Materials Studio 4.2, which was the software package used to perform all calculations.

The computational methodology used for this study is as follows. A Gaussian smearing width of each energy level is introduced to eliminate a discontinuity in the energy when an electron band crosses a Fermi level during calculation. This width is subsequently halved upon the convergence of energy values to the parameter specified by a Self-Consistent Field (SCF) condition, in which the field experienced by an atom depends on the global distribution of atoms. The calculation is then repeated and the process continues in this manner until the smearing width converges to a specific minimum value. The initial smearing width of each calculation was set to 1eV, as this value offered a reasonable compromise between speed and accuracy. It should be noted that the CASTEP graphic user interface allows for a range of values for the smearing width varying between 4.0 eV and 0.1 eV.

A pseudopotential chosen for these preliminary calculations was a norm-conserving nonlocal pseudopotential as described by Lin et al [14]. Although additional pseudopotentials are

available through the CASTEP GUI it was decided to limit these initial calculations to a single pseudopotential due to the computation time involved.

The plane wave expansion of electronic wavefunctions used by CASTEP requires the input of a kinetic cutoff energy for these wavefunctions. It was determined that specifying a cutoff energy of no less than 200 eV provided the optimum balance between computation time and precision, as cutoff energies below this value did not yield significantly varying energies. The resulting constraint on spacing of cells in reciprocal space used to generate **k**-point by a Monkhorst-Pack scheme 42 was set at 0.07 $Å^{-1}$. These parameters were employed in all calculations.

The CASTEP calculations consisted of both energy calculations for fixed structures and geometry optimizations for structures without fixed parameters. The geometry optimizations in CASTEP involve the movement of atoms in a crystal structure until a geometry is achieved that minimizes the energy. An additional investigation involved the varying of the lattice parameters resulting from each geometry optimization to within ±1Å of the optimized values to ensure the convergence of the energy to an absolute as opposed to a local minimum. This procedure was employed in all cases to test the validity of optimized lattice parameters.

For MO calculations VAMP was used on the nonperiodic version of the organic/inorganic complex. First, the energy of the optimized structure (as optimized in a periodic version of the structure by CASTEP) was calculated. A ZINDO (Zerner's Intermediate Neglect of Differential Overlap) Hamiltonian, which uses INDO to handle differential overlap, was used[15]. A full Configuration Interaction (CI) scheme, which allows all available permutations of electronic excitations in each orbital, was applied. The SCF tolerance in the calculation was $5x10^{-7}$ eV/atom (fine). Once the energy was calculated for the structure these

same constraints were applied to calculate the UV/Vis spectrum using a Gaussian integration scheme and applying a smearing width of 30 nm FWHM in order to simulate instrumental broadening.

2.2 Lattice Parameters and Electronic Density of Tin

The initial research on this topic involved computational investigation of the effect of stress on the β structure of tin. Computational results were compared with published information, and with the predictions of classical thermodynamics using published experimental data. The computational work performed so far has included quantum mechanical computations for the purpose of evaluating the crystal elastic constants of tin in the α and β structures. The results allow us to pick preferred values from among the experimentally measured values published by different authors. Comparison with data from the literature also lets this work serve as verification that the methods and input parameters used within Materials Studio will produce reasonable computed results. Materials Studio allows for the application of an applied stress on the crystal structure. The stress can be a hydrostatic pressure or a general three-dimensional stress state. The procedure used to investigate the elastic constants was to apply uniaxial pressure to an optimized Sn structure along the **(100)** direction, afterwards finding the structure that minimizes the energy of the structure while maintaining the specified stress, allowing all lattice parameters to relax to an optimum geometry. The same procedure is used to obtain an optimum lattice parameter for Sn in the BCT structure. The results of these calculations are shown in Figures 2.1 and 2.2 and are in excellent agreement with published values[16]. The intention of this series of calculations was to use the strain energy to calculate elastic stiffness constants using a finite strain or similar method.

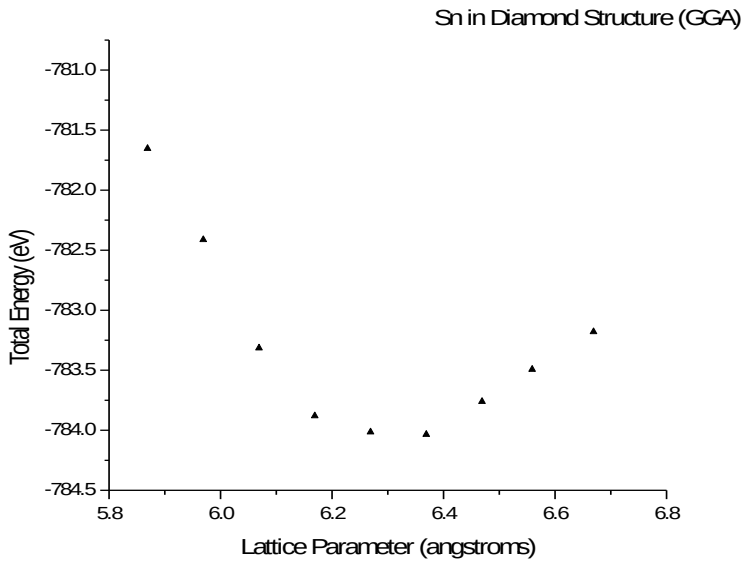

Figure 2.1
Energy as a function of lattice parameter for α-Sn

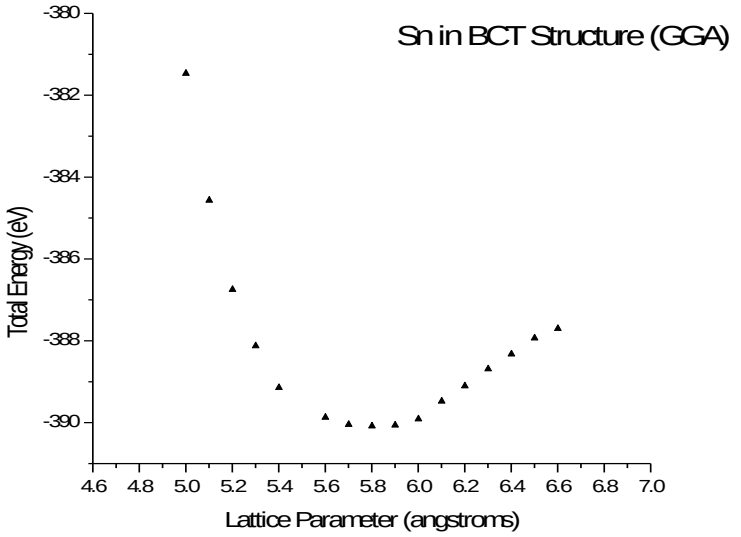

Figure 2.2
Energy as a function of the lattice parameter *c* for β-Sn

In addition to a slight discrepancy in lattice parameter between LDA and GGA calculations (approximately 0.1 Å) an interesting result is the decrease in the energy in both cases as the structure becomes compressed. In the case of LDA the structure undergoes a decrease in energy of approximately 2.5 eV from the unstressed structure and in the GGA calculation the decrease in energy is about 2.0 eV. It should be noted that this result is consistent with the overall stability of β-Sn compared to the α phase at room temperature.

An interesting observation within these findings is that the electron density seems to indicate the stability of the β structure at higher pressures. As the stress increases the band structure should evolve from one exhibiting semiconductor behavior to a more metallic structure. This is again consistent with the observed phase transformations of Sn at room temperature from diamond to BCT. Previous studies have characterized this behavior in stressed α-Sn as resulting from the increase of the occupancy of *d* orbital states (next-nearest neighbor bonds) at the cost of *s* and *p* occupancies (nearest neighbor bonds)[17]. As a result, the electron densities in the nearest neighbor regions of the lattice decrease as pressure is increased (Figures 2.3 and 2.4), seemingly in good agreement with aforementioned previous studies. It should be noted, however, that the stressed α-Sn simulations have not reached a point in which a phase transition to BCT can be exactly determined, although at a maximum stress value of 30 GPa the crystal structure matches the c/a axis ratio of that of the BCT structure.

2.3 Modeling of Organic/Inorganic Complex Pigments

Our basic approach was as follows: first, build the proposed organic/inorganic complex structure. Second, perform DFT optimizations on the structure to ensure that the arrangement is energetically favorable. Last, use a molecular orbital method to calculate the UV/Vis spectrum of

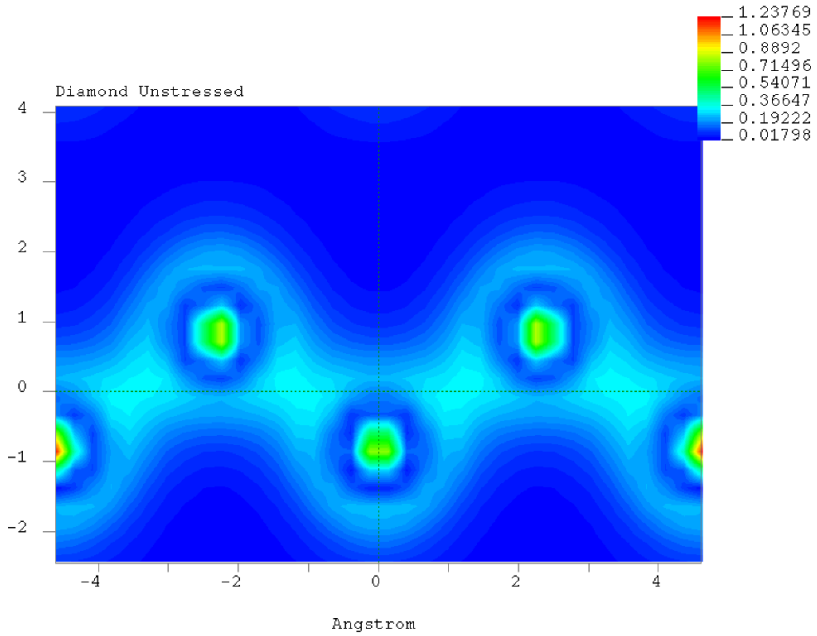

Figure 2.3
Electron density of unstressed α-Sn

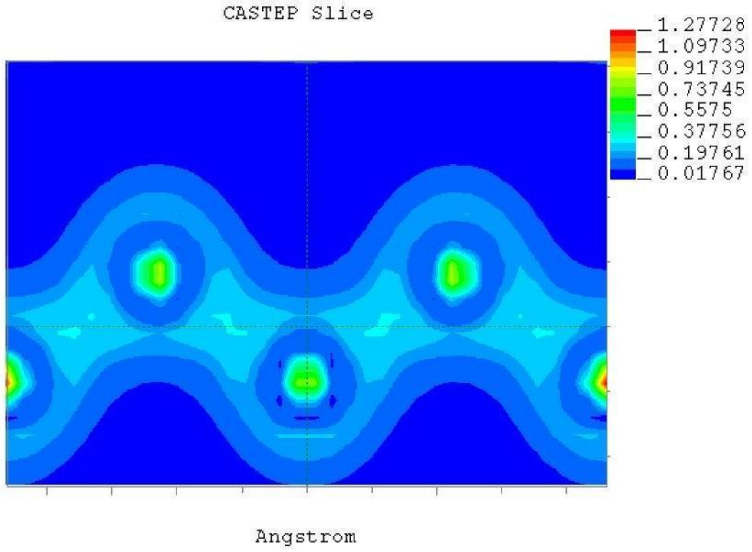

Figure 2.4
Electron density of α-Sn under 30 GPa stress

our structure and compare to experimental data. For our simulations CASTEP was used to perform the DFT optimizations and VAMP, a semi-empirical molecular orbital program, was used for calculating spectra. As our starting point we used three adjacent silica rings cut from the surface of a channel of the palygorskite structure as our substrate and then began to place individual indigo molecules within a few angstroms of the substrate (we found through trial and error that the excitations related to the UV/Vis spectrum occurred within a few angstroms of the binding site, thus eliminating the need to incorporate more of the palygorskite structure in our model, which in turn greatly reduced computational time). Simulating the surface structure was a problem in itself as CASTEP requires structures that have three dimensional periodicity. This problem was solved by creating a cubic crystal with a plane of silica rings along the plane defined by two lattice parameters and fixing the lattice parameter perpendicular to this plane as being very large (approximately 15 angstroms). This resulted in our model consisting of a series of non-interacting planes as shown in Figure 2.5, yielding the desired result. After much trial and error we found that surface structures having the following characteristics yielded the best results: binding to an aluminum defect site, pairs of molecules attaching as dimers to the palygorskite substrate, and distortion of the normally planar indigo molecule structure. An additional concern arose when in addition to the conventional indigo structure we also considered the possibility of the presence of dehydro indigo molecules. The results of the simulations are shown in Figures 2.6 and 2.7.

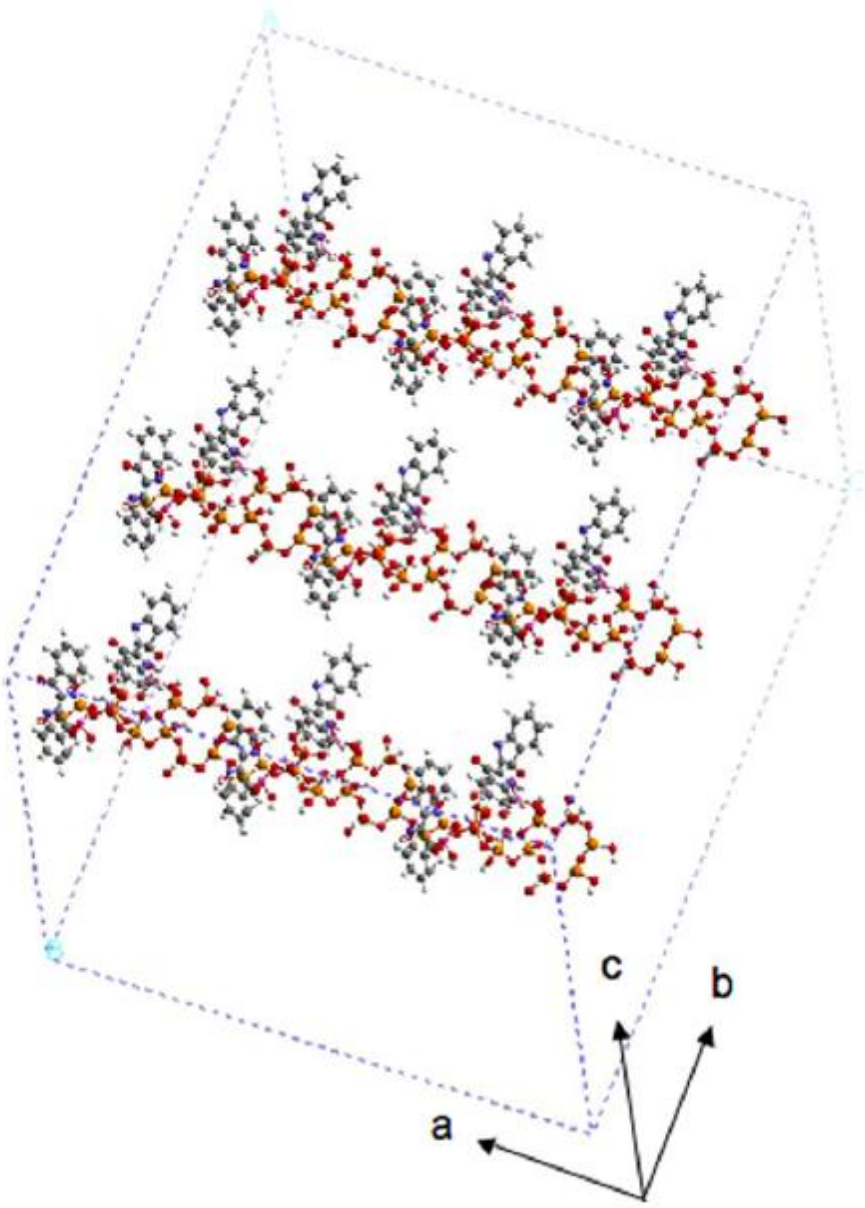

Figure 2.5

Extended cell model for DFT calculations

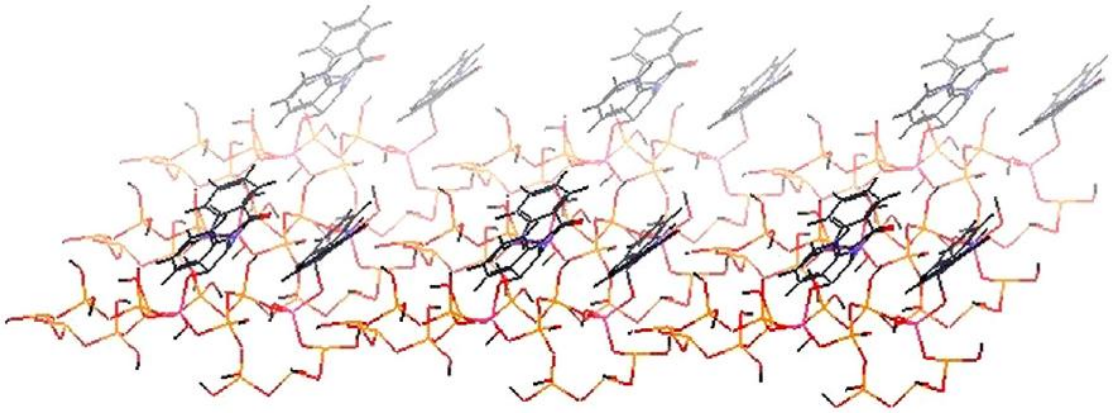

Figure 2.6
Optimized palygorskite/indigo surface complex

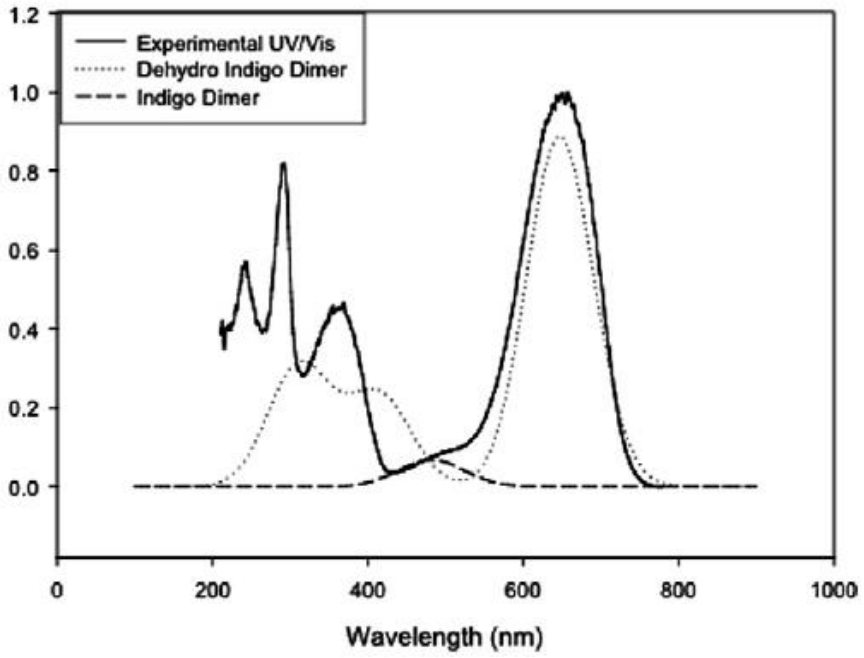

Figure 2.7
UV/Vis spectra for experimental and computational palygorskite/indigo complex

2.4 Proposed Research Objectives

The primary objectives of this research will be to employ a DFT software algorithm to determine thermodynamic and electronic parameters for a single crystal β-Sn system under varying states of mechanical stress. These parameters will then converted into crystal compliance parameters that can be compared with experimental values. Once a satisfactory degree of accuracy has been established the DFT algorithm will then be used to examine (1) the effect of varying external stress applied to the crystal structures to determine spontaneous whisker growth and (2) determination of binding site for organic/inorganic complexes (mayan pigments). Verification of computational results for the crystal structures will use published experimental data (such as UV/Vis spectra and elastic constants).

Chapter 3

BINDING SITE FOR A SEPIOLITE-BASED ORGANIC/INORGANIC COMPLEX

3.1 Introduction

Among the ruins of the Mayan civilization are many examples of murals displaying a very vivid and beautiful blue paint known as Maya Blue (figure 3.1). For more than 50 years this pigment has been the subject of much interest and debate among the scientific community[18,19]. In 1931 Merwin published photographs of the ruins of a mural at Chichen Itza, noting that a blue pigment was very distinct among the other colors present[20]. The term Maya Blue was first coined in 1946 by Gettens and Stout[21] as this pigment was believed to exist exclusively on relics of the Mayan civilization in the Yucatan Peninsula region. Since these first investigations this paint has been indentified in many other Mesoamerican artifacts found outside this region but is still known by its original designation, Maya Blue.

This fascinating material, composed of a fibrous clay material (palygorskite or sepiolite) and an organic dye (indigo) has long been renowned for its chemical stability and vivid color. Maya Blue is of great interest due to its resistance to solvents, oxidants, reducing agents, alkalis, extreme humidity, acids, and exposure to ultraviolet radiation. Even more remarkable is the fact that Maya Blue contains no heavy metal content. This material is synthesized using a very simple process involving grinding the clay, mixing with the organic dye, and heating the mixture to a temperature above the boiling point of water (typically 120 °C to 190 °C), which may have been the method used by Mayan craftsmen[22]. We now know that in addition to indigo an innumerable variety of organic dyes can be used to create a similar pigment, with the choice of the dye determining the color of the finished product[23]. This paper will propose a model for the

Figure 3.1 A photograph of a monument in Chichen Itza, Yucatan (900 C.E.), Mexico painted with Maya Blue.

binding of such a material, with the clay sepiolite being combined with the organic dye thioindigo.

3.2 Sepiolite

Sepiolite, like palygorskite, is a fibrous, colorless phyllosilicate material consisting of layers of SiO_4 tetrahedra (oriented such that unshared oxygen atoms are facing each other) bonded together with octahedrally coordinated magnesium atoms between these tetrahedral sheets[24-26]. The unit cell of the clay, shown in figure 3.2, has orthorhombic symmetry with lattice parameters a = 13.5 Å, b = 27.0 Å, c = 5.30 Å [27]. Like palygorskite, rectangular channels form parallel the c-axis of the unit cell and often contain zeolitic water or hydroxyl groups. A trivalent cation (Mn^{3+}, Al^{3+}, or Fe^{3+}) is often found as a substitutional impurity occupying a silicon site in a tetrahedral sheet[25]. Additional water is present in the octahedral magnesium layers (structural water, as opposed to zeolitic water).

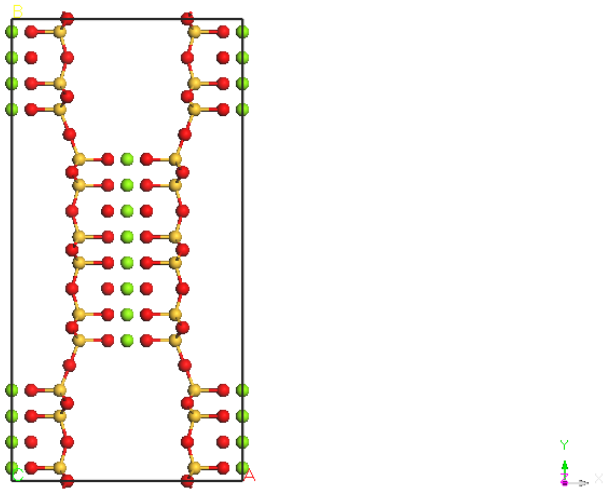

Figure 3.2 Unit cell of sepiolite, showing magnesium (green) octahedrally coordinated between chains of SiO_4 (silicon shown in orange, oxygen in white). View is along the c-axis.

The larger channel size in sepiolite compared to palygorskite makes channel diffusion and adsorption of dye molecules a more probable process in sepiolite. Ovarlez et. al.[28] found that indigo did not react with sepiolite until the clay was heated well above the boiling point of water were achieved (180 °C – 550 °C), concluding that both zeolitic and structural water groups must be removed from sepiolite before indigo bonded with sepiolite (shown in FTIR spectra). Giustetto et. al.[29] found evidence of chemical bonding between indigo and sepiolite when the clay had been heated to 190 °C (enough to remove zeolitic but not structural water) using IR and RAMAN spectroscopy, noting that a weak bond existed between the clay and C=O and N-H functional groups in indigo. Furthermore, this group concluded that this weak chemical bond could show surprising stability when formed within channels where the adsorbed indigo was difficult to reach and thus remove. In all three studies there was evidence that indigo was present in its dehydroindigo form, allowing more structural flexibility of the dye molecule. As dehyrdoindigo is a strong chemical analogue to thioindigo we expect thioindigo to diffuse and both in a similar fashion as dehyroindigo.

3.3 Color Changes in Clay/Dye Complexes

A key measure of the formation of the clay/dye complex is a dramatic color change, as shown in figure 3.3. These color changes occur only as the temperature of the clay/dye mixture is heated and a chemical interaction takes place. The blue of indigo, for example, changes to the classic Maya Blue color upon heating, a non-reversible change (a strong indication of the presence of the dehydroindigo form of the indigo molecule). Although the figure shows an example of a color change with a palygorskite/thioindigo complex these color changes have been observed for a wide range of both clays (palygorskite, sepiolite, montmorillonite) and dye molecules (indigo, thioindigo, vat orange 5, yellow 33, etc.). This color change is seen as evidence of a chemical interaction between the dye and clay, an assertion confirmed by IR and XRD spectra, HRTEM analysis, and DTA analysis[30]. An example of the color change seen in our computational model is shown in figure 3.4.

3.4 Preliminary Chemical Model for a Synthetic Sepiolite/Thioindigo Complex

Most studies on the structural characterization of sepiolite-based dye complexes have drawn a parallel with palygorskite-based complexes. For these structures, two significant and related issues are (1) whether surface biding or channel “tucking” is the predominant means of interaction, and (2) the presence of zeolitic water in these channels. The process of synthesizing sepiolite-based dye complexes involves mixing the dye with sepiolite and heating the mixture to temperatures above 120 °C, resulting in a mass loss of 6-10% in the mixture, which has been

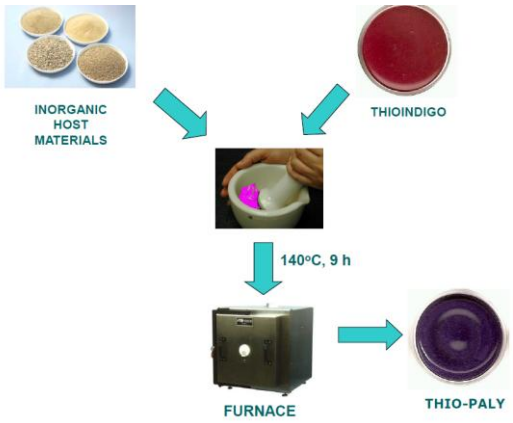

Figure 3.3 Color change of clay/dye complex during synthesis, in this case palygorskite/thioindigo

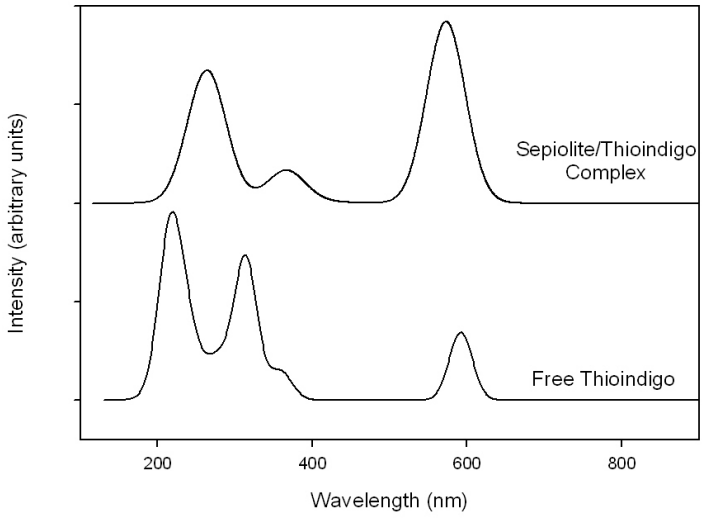

Figure 3.4 Computational color change in sepiolite-bonded thioindigo. The UV-Vis spectra are displaced vertically for clarity.

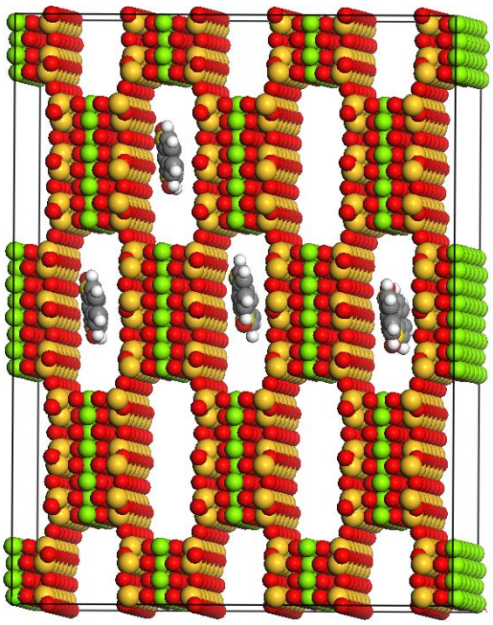

Figure 3.5 Crystal structure of sepiolite with zeolitic water removed and thioindigo tucked into several channels. Model was generated using the Sorption module in Materials Studio version 4.2.

attributed to loss of zeolitic water molecules by thermogravimetric analysis (TGA)[31]. Although sepiolite has been observed to undergo structural collapse and loss of channels with removal of structural water[32] the temperatures required to achieve this (approximately 800 °C) are far in excess of the temperatures used in the synthesis of this material. We therefore proceed on the assumption that the channels in sepiolite are clear of water and are capable of having thioindigo molecules diffusing into these channels, as the channel size is more than large enough to accommodate the dye molecule. Having thioindigo instead of indigo as the dye component of the complex does simplify the problem in that we do not have to deal with indigo's active chemistry at elevated temperatures. Our preliminary chemical model is shown in figure 3.5.

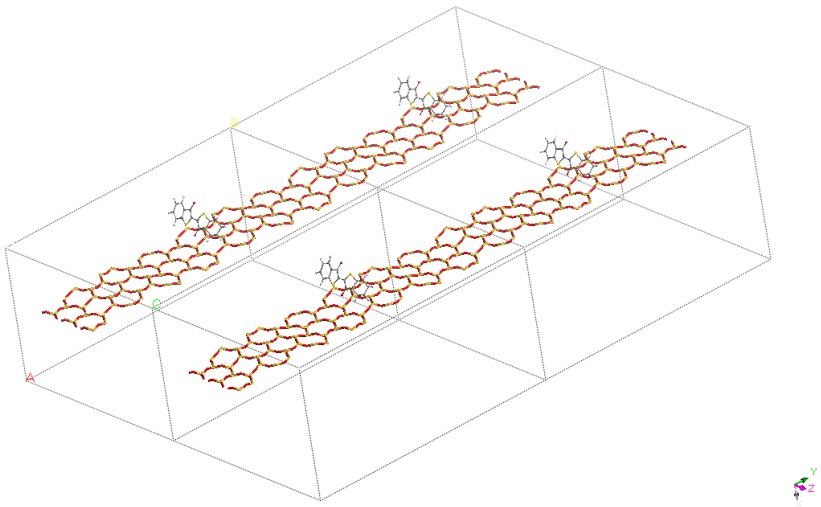

Figure 3.6 Periodic structure of Sepiolite/thioindigo complex used for CASTEP calculation

3.5 DFT and MO Results for Calculation of Optical Spectra

We modeled the sepiolite-thioindigo system by first optimizing the structure geometry using a plane-wave pseudopotential DFT code, CASTEP[33], and then calculating the optical spectrum using a molecular orbital (MO) method, VAMP[34]. The proposed structures (with approximate geometries provided by the Sorption module[35] in Cerius[2] as a starting point) were modeled as a surface by taking a 14x3 lattice of adjacent silica rings (mimicking the morphology along a wall of a channel in sepiolite) and introducing a substitutional impurity at a silicon site (based on spectroscopic data, aluminum, iron, and magnesium were used in our simulations). Using this proposed surface complex as a basis we constructed a three dimensional unit cell as required by CASTEP for geometry optimizations (figure 3.6). By allowing the unit cell to have a very large lattice parameter perpendicular to the surface we are able to simulate a surface interaction while satisfying three dimensional periodicity required by CASTEP as the simulation becomes one of modeling a series of noninteracting parallel planes (confirmed by the fact that the total electronic energy converged to a constant value as this lattice parameter is increased).

Once the model converged to an optimum geometry by CASTEP using a generalized gradient approximation (GGA) functional the structure is reduced to a non-periodic structure (required for a VAMP calculation) consisting of 3 adjacent silica rings and the attached dye molecule as structures larger than this were prohibitively expensive in terms of computational power. A VAMP molecular orbital simulation employing a neglect of diatomic differential overlap (NDDO) Hamiltonian with a full configuration interaction (CI) scheme was then used to calculate UV/Vis spectra and compare to experimental data. This process was repeated using single and multiple substitutional metallic impurity sites using the aforementioned metals found in sepiolite as well as monomer, dimer, and trimer thioindigo complexes. We found the best agreement between computational and experimental spectra when the structures had the following characteristics:

- Tetrahedral bonding of thioindigo to an aluminum impurity site
- A single thioindigo molecule bonded to an aluminum site in the nonperiodic surface mesh
- Distortion of the thioindigo molecule from its planar structure. This has been associated with the observed color changes in the synthesis of mayan pigments and related materials[30]

The first two observations ran contrary to our findings with a palygorskite/thioindigo complex, which saw the best UV/Vis spectral fit for octahedral binding and a dimer thioindigo structure attaching to the surface mesh. The results for the optical spectrum for the thioindigo/sepiolite complex are shown in figure 3.7, showing excellent agreement in both

visible and near-UV regions between the computational and experimental results (a sampling of UV/Vis results for different impurity species is shown in figure 3.8). The optimized molecular structure corresponding to this result is shown in figure 3.9. Two interesting features of this structure are (1) unlike palygorskite-based mayan pigments which display a dimer structure on the adsorbed dye molecules, only a single dye molecule bonds to the surface mesh, and (2) the dye molecule is bonded to the surface via a Van der Waals interaction. While such an interaction would seem to be at odds with the resistance to color fading of mayan pigments we must consider the added stability of channel bonding sites within the clay as due to physical confinement of the dye molecules within these channels in a manner analogous to layer intercalation in catalytic materials such as MoS_2[36]. An additional argument in support of channel bonding is the fact that the maximum concentrations of dye are less than those possible in palygorkite-based complexes[37] in which the dye is known to bond to the clay predominantly at surface sites.

3.6 Conclusions

In this paper we have presented a model for the chemical interaction between sepiolite and thioindigo in a clay/dye complex similar in nature to palygorskite/dye based Mayan pigment complexes. During synthesis sepiolite loses its zeolitic water content, opening up channels for the insertion of thioindigo molecules. The experimentally reported concentration of dye in this complex is consistent with channel absorption of the dye. Thioindigo attaches to the channel at an aluminum impurity site, with an additional but noninteracting aluminum impurity site nearby. The interaction is of a Van der Waals nature. The simulated model showed a significant distortion of the planar geometry of thioindigo, a characteristic of the well known

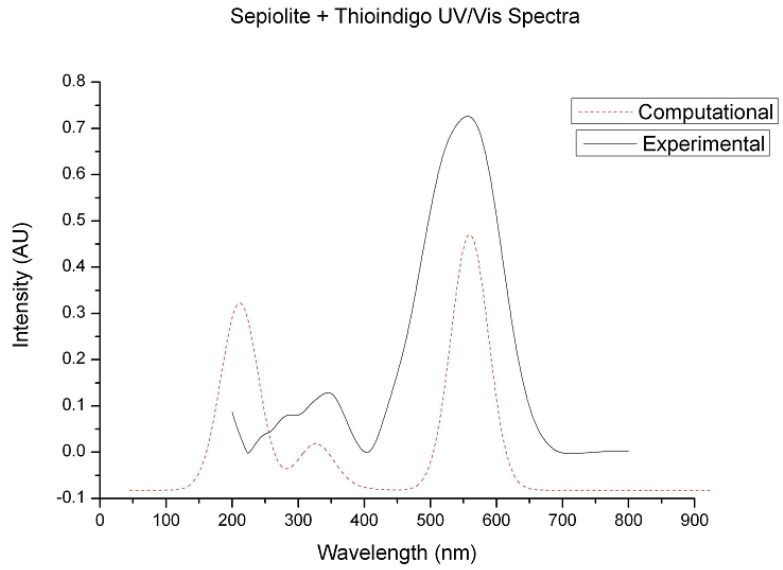

Figure 3.7 Comparison of computational and experimental UV/Vis spectrum of the thioindigo/sepiolite complex

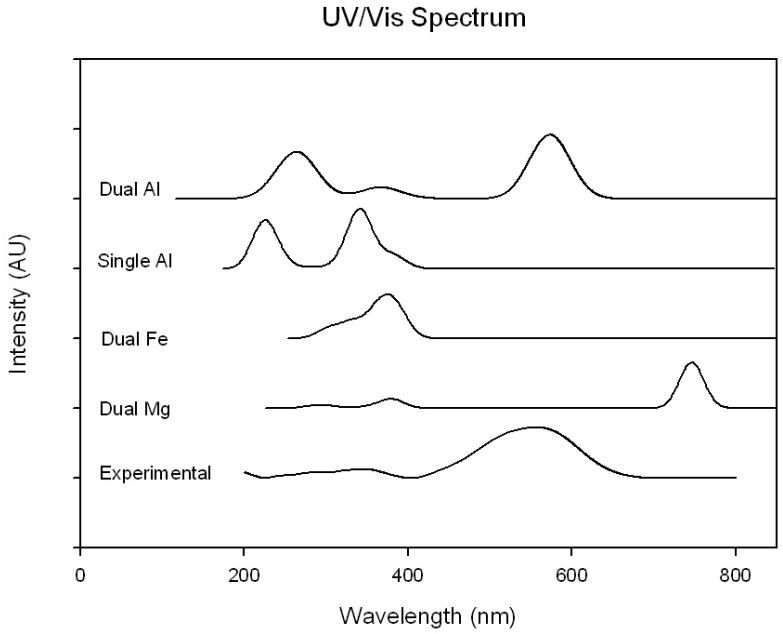

Figure 3.8 Sampling of UV/Vis spectrum of the thioindigo/sepiolite complex using different impurity species.

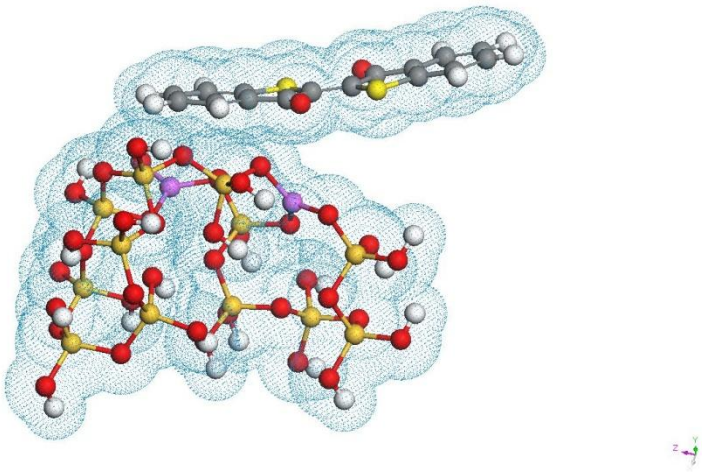

Figure 3.9 Optimized thioindigo/sepiolite structure with Van der Waals surface displayed. Note the distortion of the planar geometry of the thioindigo molecule.

color changes in Mayan pigment type materials. The UV/Vis spectrum of the model was simulated using both DFT and MO methods and is in excellent agreement with experimental results for the spectrum. Future studies will develop a model for a sepiolite/indigo complex.

Chapter 4

DFT CALCULATIONS OF ELASTIC CONSTANTS IN β-Sn

4.1 Introduction

The total internal energies of the stressed crystal structures can be converted into crystal compliance parameters using the method outlined by Kittel[16] assuming that the appropriate orientations of the applied stress are used. CASTEP can be used to calculate elastic constants using a finite strain technique, in which a homogeneous strain is applied to a unit cell and the corresponding stress is then calculated (this is much less computationally expensive than using the stress to calculate a strain, as in the finite strain method no cell optimization is required). The finite strain method uses a small amount of strain in a given orientation (small enough such that the geometry of the structure remains unchanged) in order to calculate a stress tensor and subsequently the total energy of the structure. This method has been used successfully in calculating the elastic constants of a variety metals, minerals, and semiconductors[38-42]. Table 1 shows the results of this calculation when compared to prior experimental studies[43,44] which used a static method (Bridgman) or an acoustic method (Mason and Bommel). Although the parameters we obtained seem to be in general agreement with the published results, there are discrepancies between the numbers previously published. The computed values are of reasonable magnitude and may be as dependable as the experimental data. All three sets of elastic stiffness constant values will be used in the computations of the proposed research.

Table 4.1 Elastic Stiffness Constants of β-Sn

Authors	Elastic Stiffness Constants in 10^{11} Pa					
	c_{11}	c_{33}	c_{44}	c_{66}	c_{12}	c_{13}
Bridgman	8.39	9.67	1.75	0.741	4.87	2.81
Mason and Bommel	7.33	8.74	2.19	2.25	2.38	2.48
Alvarado	6.80	8.68	3.15	1.72	3.45	2.97

4.2 Elastic Energy Density Calculations

One possible application of elastic energy calculations is Lee and Lee suggest that the orientation of surface grains plays a very significant factor in spontaneous tin whisker growth[45] and go on to catalog the preferred orientation of grains from which whiskers tend to grow. One aspect of the orientation dependence is the orientation-sensitive strain energy available to drive whisker growth. Kinetic factors (such as dislocation climb rates and self-diffusion rates within a crystal) will also be dependent on orientation. It is interesting to evaluate whether the strain-energy orientation dependence would by itself dictate which grain orientations grow whiskers. However, published elastic constants for tin are somewhat inconsistent. CASTEP allows for DFT-based calculation of elastic constants, so that we can try theoretical as well as experimental crystal stiffnesses to calculate the energy resulting from an applied stress. CASTEP applies a finite strain technique to calculate the elastic constants of a material based on energy differences generated as a result of a series lattice strains[46]. In our case, we use an equibiaxial stress of 1 Pa in the plane of the film and zero stress normal to the film. Then the appropriate rotation matrix operation can be used to project the stress onto the specific orientation of the surface grain. The resultant elastic strain energy density can thus be calculated as a function of grain orientation for a given stress. These results are shown in Table 2. In the table, the grain

Table 4.2 Elastic energy density as a function of grain orientation

Elastic Energy Densities in J/m^3

Grain Orientation	Bridgman	Mason and Bommel	Alvarado
[220]	2.0×10^{-12}	1.1×10^{-12}	1.1×10^{-12}
[420]	1.9 x 10-^{12}	1.4×10^{-12}	1.0×10^{-12}
[620]	1.9×10^{-12}	1.1×10^{-12}	0.89×10^{-12}
[501]	2.0×10^{-12}	1.2×10^{-12}	1.0×10^{-12}
[321]	2.1×10^{-12}	1.4×10^{-12}	0.91×10^{-12}
[100]	2.7×10^{-12}	1.8×10^{-12}	1.4×10^{-12}
[111]	2.4×10^{-12}	1.3×10^{-12}	0.88×10^{-12}
[113]	2.4×10^{-12}	1.7×10^{-12}	1.8×10^{-12}
[211]	2.2×10^{-12}	1.6 x 10-^{12}	2.0×10^{-12}
[212]	2.1×10^{-12}	1.6×10^{-12}	2.0×10^{-12}

orientations which Lee and Lee have observed to favor whisker growth are shown in bold font (orientations are specified as the crystal direction normal to the surfaces of the film.) Overall, orientations of grains that favor whisker growth do have elastic energy densities which are lower than those of the grains that did not grow whiskers (although this difference may not be very large). However, the trend is imperfect: for example, the [111] orientation (using the Alvarado stiffness values) has the lowest strain energy of all the computed values.

An additional application of computational elastic constants is the calculation of elastic energies as a result of hydrostatic pressure. Besides the problem of metal fatigue, these energy calculations can be useful in investigating stress-induced allotropic transformations, such as the $\alpha \rightarrow \beta$ transition in Sn. Table 3 shows the elastic energy density resulting from a hydrostatic pressure of 1 Pa applied to the β-Sn structure, using the three sets of elastic stiffness constants

Table 4.3 Elastic energy densities resulting from the application of 1 Pa hydrostatic stress

Author	Elastic Energy Density (J/m^3)
Bridgman	8.90×10^{-12}
Mason and Bommel	5.94×10^{-12}
Alvarado	2.07×10^{-11}

listed in this chapter (calculated again using the Hooke's Law approach outlined in Kittel[16]).

4.3 Conclusions

Although the computational energy density values are within a factor of 3 there remains enough discrepancy that may indicate other factors may be taken into consideration in order to give better agreement. One important consideration is the fact that the published values of the elastic stiffness constants were taken by different methods, as Bridgman measured using a static technique whereas Mason took ultrasonic measurements and as such there is a significant difference between the published values). Another factor to take into account is the fact that thermal effects were not considered in the calculation. Rayne and Chandrasekhar[47], using an ultrasonic technique, measured the dependence of elastic stiffnesses on temperature as shown in figure 4.1 for c_{11}. A DFT calculation is not able to incorporate temperature effects directly other than adjusting the lattice parameter to reflect the temperature corresponding to the published data and thus this remains a problem that might be solved by using a Molecular Dynamics package to simulate a change in temperature followed by a DFT calculation of the elastic constants for the

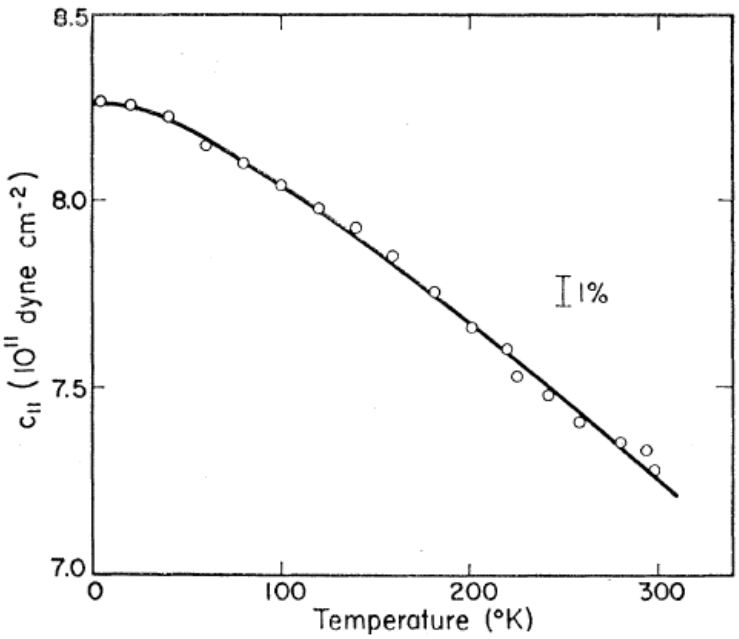

Figure 4.1 Dependence of elastic stiffness constant c_{11} on temperature, from reference 47.

structure. As DFT has no allowance for temperature effects other than the setting of a lattice parameter to reflect the value at a known temperature, this method would be ideally suited for calculating elastic constants at 0 K. However, since the simulation imposed room temperature lattice parameters (CASTEP imposes this restriction for stress calculations) it is not surprising that our c_{ij} values are a poor match for the Rayne and Chandrasekhar low temperature values (measured at T = 4.2 K).

The comparison between our calculated values and those of published data shows a great deal of inconsistency. The values of C_{11}, C_{33}, $C_{44,}$ and C_{66} are in good agreement between the papers of Rayne and Chandrasekhar and of Mason and Bommel, but there is no agreement on C_{12} and C_{13}. Bridgman's values differ from all the other studies, which may be a reflection of the different measurement method Bridgman used (static vs acoustic). The use of different sets of elastic constants could easily lead to significant differences in strain energy densities and

could cloud the issue in any studies of stress- and strain-related phenomena such as whisker growth, allotropic structure transformation, and thermodynamic stability of thin films. Therefore, further work is needed, in order to clarify the elastic constants of tin.

CHAPTER 5 SUMMARY AND CONCLUSIONS

5.1 Summary

Two problems were studied using DFT. First, palygorksite and sepiolite-based Mayan pigments were modeled and had energies calculated using DFT software, with the specific binding sites of dye molecules and the species of impurity cation present in the clay structure varied until the UV/Vis spectrum of the structure matched that of experimental and published data. Second, DFT was used to calculate lattice parameters and elastic constant data for β-Sn, with the results being compared to a variety of experimental and published results. Our specific conclusions are listed as follows for both types of calculations.

5.2 Conclusions from Mayan pigment calculations

- In both palygorskite and sepiolite-based Mayan pigments, tetrahedrally-coordinated aluminum is the impurity cation present in the clay structure
- Palygorkite-based pigments have the dye molecules (indigo, thioindigo) bind to the surface in a dimer geometry. This implies that the predominant binding site occurs at the surface of the clay, as the concentration of the dye present as well as the physical space required for dimer indigo/thioindigo molecules to attach to the clay rule out the possibility of channel binding.
- Both indigo and dehydro indigo are present in Mayacrom Blue.
- Sepiolite-based pigments have a single dye molecule (thioindigo) attaching to an aluminum site in the clay structure. An additional tetrahedral aluminum must be present in a nearby site in order to match the experimental UV/Vis spectrum.

- As a much lower concentration of indigo is present in a sepiolite-based dye than in the palygorskite-based dye we believe that channels sites are being occupied. This is made possible by the wider channels in sepiolite as well as a single dye molecule attaching to aluminum sites as opposed to dimer bonding.

5.3 Conclusions from Calculations of Elastic Constants in β-Sn

- DFT can be used to evaluate the dependence of lattice energy on lattice parameters for the β-Sn structure. By measuring the dependence of energy on an applied strain elastic stiffness values can be extracted from this type of calculation.
- The DFT program CASTEP, using a finite strain calculation, can provide C_{ij} values for the elastic stiffness tensor of tin. These values would be relevant at temperatures near absolute zero. However, comparing the computational results with experimental values of Rayne and Chandrasekhar, the agreement with T=4.2 K data is no better than the agreement with the T=300 K data.
- The inconsistencies among published elastic constants for white tin are not resolved by the computations reported here. The values of C_{11}, C_{33}, $C_{44,}$ and C_{66} are in good agreement between the papers of Rayne and Chandrasekhar and of Mason and Bommel, but there is no agreement on C_{12} and C_{13}. Bridgeman's values of all six stiffnesses are inconsistent with other studies. The values from the present DFT study are also at odds with the reported experimental data, including the T=4.2 K data of Rayne and Chandrasekhar.
- Use of the different, discordant sets of elastic stiffness values would lead to significant discrepancies in calculated strain energy densities for beta tin. These discrepancies

would cloud the issue in any studies of stress- and strain-related phenomena such as whisker growth, allotropic structure transformation, and thermodynamic stability of thin films. Therefore, further work is needed, in order to clarify the elastic constants of tin.

REFERENCES

1. E. Teller, *Rev. Mod. Phys.* **34,** 627 (1962).
2. W. Kohn and L. J. Sham, *Phys. Rev.* **140,** 1133A (1965).
3. L. H. Thomas, *Proc. Cambridge Phil. Soc.* 23, 542 (1927).
4. E. Fermi, *Rend. Accad. Naz. Lincei* 6, 602 (1927).
5. D. C. Langreth and M. J. Mehl, *Phys. Rev. Lett.* **47**, 446 (1981).
6. M. C. Payne, M. P. Teter, D. C. Allan, T. A. Arias, and J. D. Joannopoulos, *Rev. Modern Phys.* **64,** 1045 (1992).
7. M. P. Teter, D. C. Allan, M. C. Payne, *Phys. Rev. B* **40,** 12255 (1989).
8. R. Car, M. Parrinelo, *Phys. Rev. Lett.* **55,** 2471 (1985).
9. E. Hückel, *Zeitschrift für Physik* **70**, 204 (1931).
10. J. A. Pople and Sir J. Lennard-Jones, *Proc. Roy. Soc.* **A 202,** 166 (1950).
11. A. Zunger and A. J. Freeman, *Phys. Rev. B* **15**, 4716 (1977).
12. J. A. Pople and G. A. Segal, *J. Chem. Phys.* **43**, S136 (1965).
13. J. A. Pople, D. L. Beveridge, and P. A. Dobosh, *J. Chem Phys.* **47**, 2026 (1967).
14. I. Stich, M. C. Payne, R. D. King-Smith, J-S. Lin, and L. J. Clarke, *Phys. Rev. Lett.* **68** (9), 1351 (1992).
15. M. Zerner, Reviews in Computational Chemistry, Volume 2, Eds. K. B. Lipkowitz and D. B. Boyd, VCH, New York, 313, (1991).
16. C. Kittel, *Introduction to Solid State Physics*, John Wiley, New York (1995).
17. E. Hückel, *Zeitschrift für Physik* **70**, 204 (1931).
18. M.J. Yacaman and M. C. S. Puche, *Mater. Res. Soc. Symp.* **352,** 3 (1995).
19. R. Kleber, L. Masschelein-Kleiner, and J. Thissen, *Stud. Conservat.* **12,** 41 (1967).

20. H.E. Merwin, in: Yucatan, H.E. Morris, J. Charlot, A.A. Morris (Eds.), *Temple Warriors at Chitzen Itza*, 406, Carnegie Institution of Washington, Washington, DC, 1931, p. 356.

21. R.J. Gettens, G.L. Stout (Eds.), *Paint Materials: A Short Encyclopedia*, D. van Nostrand, New York, NY, 1946.

22. H. V. Olphen, *Science* **154,** 645 (1966).

23. R. R. Chianelli and L. A. Polette, US Patent 7,052,541, May 30, 2006.

24. A. Alvarez, *Palygorskite-sepiolite: Ocurrences, Genesis, and Uses*, New York, Elsevier, 253.

25. D. L. Bish and G. D. Guthrie Jr., *Rev. Min.* **28,** 139 (1993).

26. K. Hansen and B. T. Mossman, *Cancer Res.* **47,** 1681 (1987).

27. G. W. Brindley, A*m. Miner.* **44,** 495 (1959).

28. S. Ovarlez, F. Giulieri, F. Delamare, N. Sbirrazzuoli, A. M. Chaze, *Micro. And Meso. Mater.* **142,** 371 (2011).

29. R. Giustetto, K. Seenivasan, and S. Bordiga, *Per. Mineral. Special Issue,* 21 (2010).

30. L. A. Polette-Niewold, F. S. Manciu, B. Torres, M. Alvarado, and R. R. Chianelli, *J. Inorg. Biochem*. **101**, 1958 (2007).

31. S. Ovarlez, A. M. Chaze, F. Giulieri, and F. Delamare, *C. R. Chemie* **9,** 1243 (2006).

32. J. J. Beaudoin and P. E. Grattan-Bellew, *Cement and Concrete Res.* **10** (3), 347 (1980).

33. M. C. Payne, M. P. Teter, D. C. Allan, T. A. Arias, and J. D. Joannopoulos, *Rev. Mod. Phys.* **64** (4), 1045 (1992).

34. J. Hafner, *J. Comp. Chem.* **29,** 2044 (2008).

35. N. Metropolis, A. W. Rosenbluth, M. N. Rosenbluth, A. H. Teller, and E. J. Teller, *J. Chem. Phys.* **21,** 1087 (1953).

36. K. E. Dungey, M. D. Curtis, and J. E. Penner-Hahn, *Chem. Mater.* **10,** 2152 (1998).

37. S. Ovarlez, A. M. Chaze, F. Giulieri,and F. Delamare, *A chemical comprehension of the colour centres in Maya blue green palette. A study of indigo chemisorption in sepiolite,* Dyes in History and Archaelogy Conference, Suceava, Romania; 2006.

38. Karki, B. B.; Clark, S. J.; Warren, M. C.; Hsueh, H. C.; Ackland, G. J.; Crain, J., *J. Phys.: Cond. Matt.*, **9**, 375 (1997).

39. Karki, B. B.; Stixrude, L.; Clark, S. J.; Warren, M. C.; Ackland, G. J.; Crain, J., *Am. Mineral.*, **82**, 635 (1997).

40. Milman, V.; Warren, M. C., *J. Phys.: Condens. Matter* **13**, 5585 (2001b).

41. M. Jose-Yacaman and M. C. S. Puche, *Mater. Res. Soc. Symp.* **352**, 3 (1995).

42. R. Kleber, L. Masschelein-Kleiner, and J. Thiessen, *Stud. Conservat*. **12**, 41 (1967).

43. W. P. Mason and H. E. Bommel, *J. Acoust. Soc. Am.* **28**, 930 (1956).

44. G. S. Baker, *Acta metal.* **5**, 353 (1957).

45. B. Z. Lee and D. N. Lee, *Acta. Mater.* **46,** 3701 (1998).

46. L. Fast, J. M. Wills, B. Johansson, and O. Eriksson, Phys. Rev. B **51**, 17431 (1995).

47. J. A. Rayne and B. S. Chandrasekhar, *Phys Rev B* **120**, 1658 (1960)

CURRICULUM VITA

Manuel Alvarado Jr. was born on May 3, 1970 in El Paso, TX, the eldest child of Manuel Alvarado Sr. and Eva Alvarado. He graduated from Socorro High School in El Paso, TX in 1988. He received his Bachelor of Science degree in Physics in 1994 and his Master of Science degree in Physics in 1997, both from the University of Texas at El Paso (UTEP). He is pursuing doctoral studies in Materials Science and Engineering at UTEP under the guidance of Dr. Roy Arrowood, during which he was awarded the Dodson Doctoral Fellowship. He has served as an associate researcher with the Materials Research and Technology Institute (MRTI) under Dr. Russ Chianelli. He is currently a faculty member in the Department of Physics at El Paso Community College (EPCC) and is a Senior Engineer at TXL Group in El Paso, TX.